

STAGNATION FLOW IN STREAMER BOUNDARIES

S. T. SUESS

NASA Marshall Space Flight Center, SD50, Huntsville, AL 35812; steve.suess@msfc.nasa.gov

AND

S. F. NERNEY

Department of Physics, Ohio University, Lancaster, OH 43130

Received 2001 August 11; accepted 2001 September 28

ABSTRACT

Flow tubes adjacent to closed magnetic field lines on the boundaries of streamers can have spreading factors that change rapidly with height. Numerical models in this thin layer are subject to uncertainties. Here we use an analytic model of magnetically closed and adjacent open regions to compute the spreading factor close to the closed field lines and the flow on the open field lines. We are able to recover the shape of the closed field region, or helmet, and show the evolution of the helmet under slowly increasing temperature. We also show why and when stagnation flow can occur in the vicinity of the cusp at the top of the helmet.

Subject headings: MHD — Sun: corona — Sun: magnetic fields

1. INTRODUCTION

We describe a model of slow solar wind flow in streamer boundaries in the solar corona. It is an essentially analytic model based on early work by Pneuman (1968, hereafter P68), but applied in a new way and extended. We show new solutions illustrating the maximum heights of the closed magnetic field regions (the helmets) in streamers, the evolutionary changes in streamers under increasing temperature, and the stagnation flow that occurs in the vicinity of the magnetic cusp at the top of the helmet (Vásquez et al. 1999). This is a mathematically simple but physically rich model that can be applied to the analysis of several physical processes without the complexity inherent in multidimensional MHD models.

Slow solar wind originates from coronal streamers in a way that is not understood but for which several hypotheses exist. The model described here is based on the hypothesis that the flow geometry adjacent to the helmet plays an important role in the origin of the slow flows. Specifically, we examine flow between the helmet and the streamer brightness boundary, so named because this is the boundary between a bright streamer and an adjacent coronal hole. This sharp boundary in density is often visible to $30 R_{\odot}$, while the last closed field lines in the helmet never extend above $4.0 R_{\odot}$ and probably not even above $2.5 R_{\odot}$ (Suess et al. 1999b; Wang et al. 1998). Therefore, the brightness boundary defines a density boundary in expanding solar wind. Since slow wind is found empirically to be denser than fast wind, it is logical to conclude that the brightness boundary is the fast-/slow-wind boundary in the corona. Figure 1 shows negative and positive images of the corona during the 1973 solar eclipse. Several brightness boundaries are visible in a group of overlapping streamers on the west limb. Boundaries A and B are examples of typical sharp boundaries. Streamer C is a well-defined isolated streamer, and we show schematic field lines in C on the right suggesting how the helmet might appear inside the streamer.

In § 2 we give a physical description of the model and describe the assumptions made to arrive at this model. In § 3 we give the corresponding mathematical description of the model, and in § 4 we show several different solutions,

first extending the P68 results and then illustrating stagnation flow near the helmet cusp. Sections 5 and 6 contain discussions of these solutions and, more generally, of the model itself. Section 7 is a brief summary.

2. ASSUMPTIONS AND PHYSICAL DESCRIPTION OF THE MODEL

The model is based on the property of streamers that the ratio of thermal pressure to magnetic pressure, $\beta \equiv 8\pi p/B^2$, is greater than unity ($\beta > 1$) in the helmet above $\sim 1.2 R_{\odot}$ (p is pressure, B is magnetic field strength). We begin by giving the basis for this result and then go on to show how it can be applied.

Empirically, β is estimated by measuring temperatures and densities and using a model to estimate the coronal magnetic field strength, which is presently impossible to measure directly. Li et al. (1998) did this using the *Solar and Heliospheric Observatory* Ultraviolet Coronagraph and Spectrometer (SOHO/UVCS) and *Yohkoh* Soft X-Ray Telescope (Yohkoh/SXT) measurements. They analyzed a coronal helmet streamer observed on 1996 July 25, which was stable from July 22 to 27 July, and derived the temperatures and densities at 1.15 and $1.5 R_{\odot}$, as shown in Table 1. Density was compared with a hydrostatic isothermal equilibrium model and a hydrostatic equilibrium plus thermal conduction model. They concluded that the streamer was in hydrostatic equilibrium and isothermal within experimental uncertainty in the closed field regions. Li et al. (1998) estimated the magnetic field strength according to the potential field calculation described in Raymond et al. (1998). The extrapolation was based on the National Solar Observatory (NSO)/Kitt Peak synoptic maps of the magnetic field for the month of 1996 July, along with the assumption of a source surface at $2.5 R_{\odot}$. The inferred field strength was 0.55 G at $1.15 R_{\odot}$ and 0.21 G at $1.50 R_{\odot}$. The resulting plasma β was $\beta = 5$ at $1.15 R_{\odot}$ and $\beta = 3$ at $1.50 R_{\odot}$. The conclusion was that gas pressure is important in the closed field region. It can be seen that the magnetic field in this streamer falls off quite rapidly with height, and this is generally the case for streamers since the field is a multipole with closed loops. Because of this, the field is weaker inside

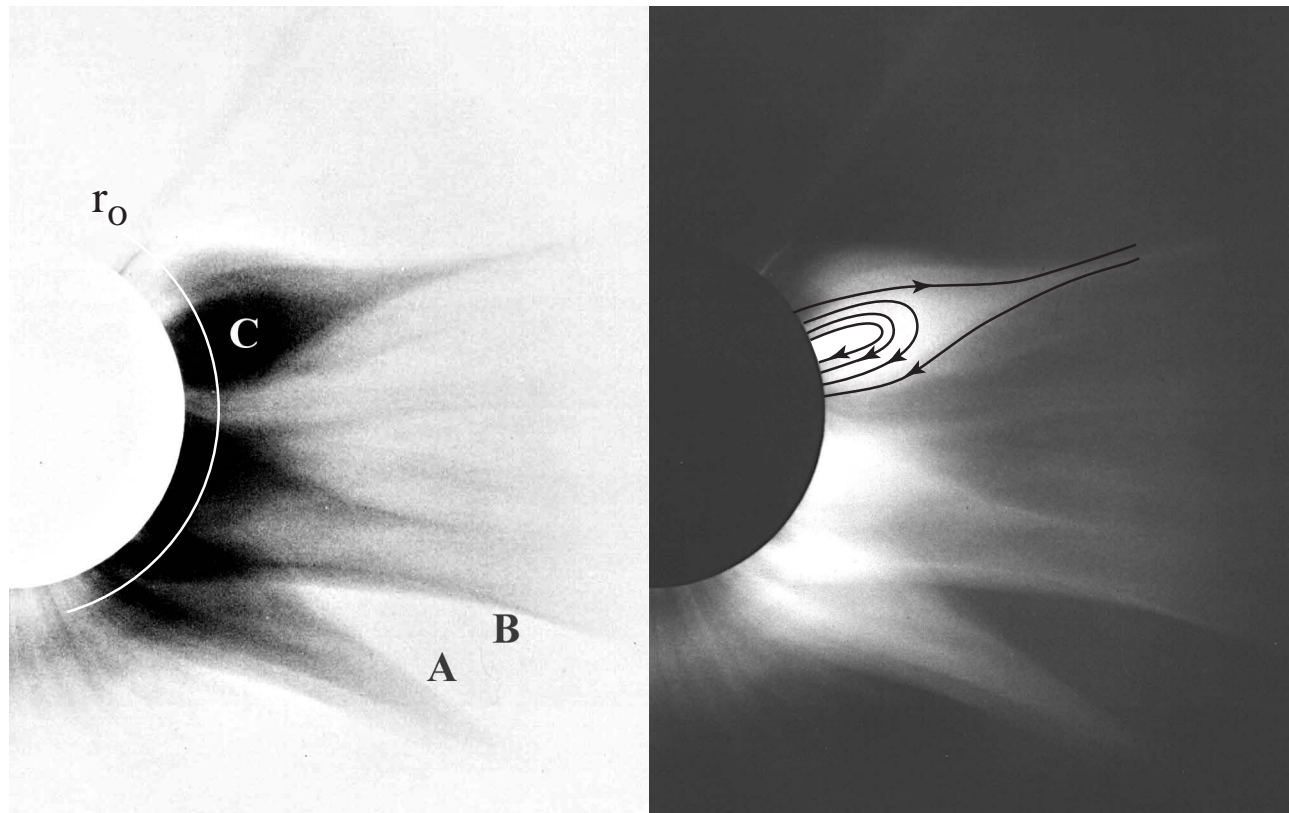


FIG. 1.—1973 eclipse images from the west limb (courtesy of G. Newkirk and HAO) showing a complex of overlying streamers. The same image is plotted in both negative (*left*) and positive (*right*). Streamers (e.g., C) are regions in and above closed field lines, shown schematically in the right panel, above a photospheric neutral line. Streamer brightness boundaries (e.g., A, B) are extremely sharp and can often be seen to at least $20 R_{\odot}$. As discussed in the text, $\beta > 1$ in and above streamers above some height r_0 that is no more than $1.2 R_{\odot}$.

a helmet than outside, except perhaps at low heights above an active region (Suess, Gary, & Nerney 1999a; Gary 2001). This empirical result is consistent with and, in fact, is preceded by several numerical simulations that are unanimous in predicting streamers with $\beta > 1$ throughout the closed field region and upward to several solar radii. Typical numerical models of global coronal structure today begin with specified boundary values for the magnetic field and plasma variables, a potential magnetic field in the corona, and spherically symmetric outflow. The configuration, which is initially not in equilibrium, is then allowed to relax in time until it is changing slowly compared to a coronal expansion time. A well-known early example of this type of model is that of Steinolfson, Suess, & Wu (1982), which gives $\beta \geq 1$ from the base upward everywhere within and above the closed field region. Modern models reproduce coronal temperatures, densities, and flow speeds in both coronal holes and streamers very well using volumetric energy and heating sources. Figure 2 illustrates one such model (Wang et al. 1998) that is typical in terms of the result that $\beta \geq 1$ in the helmet while $\beta \ll 1$ in the adjacent

coronal hole—a well-established empirical property of coronal holes. The results in Figure 2 show that the magnetic field can be neglected inside the helmet to order 1 ($O[1]$) everywhere above $1.2 R_{\odot}$ and to even lower heights when there are no active regions (Gary 2001). This result was anticipated in P68, where the magnetic field inside the helmet had been neglected in an early streamer model.

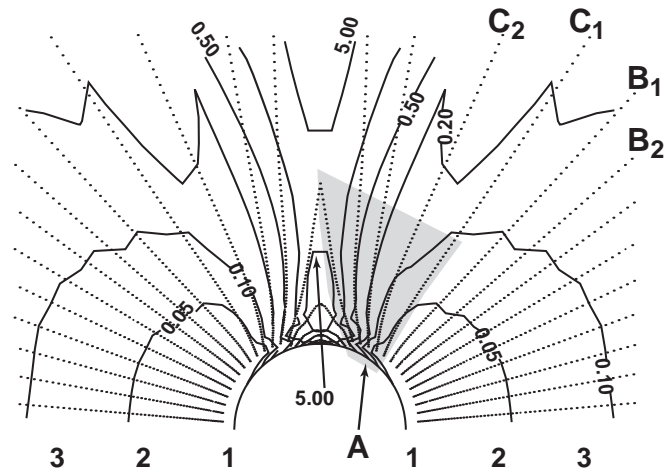


FIG. 2.—Plasma β distribution in a streamer and adjacent coronal holes from the two-fluid MHD model of Suess et al. (1999c). The radius scale at the bottom is in solar radii. Magnetic field lines are shown as dotted lines.

TABLE 1
STREAMER ELECTRON TEMPERATURE AND DENSITY

Height	$1.15 R_{\odot}$	$1.50 R_{\odot}$
Temperature.....	1.9×10^6 K	1.6×10^6 K
Density.....	1.23×10^8 cm $^{-3}$	1.26×10^7 cm $^{-3}$

NOTE.—From Li et al 1998.

The geometry of the P68 model is shown in Figure 3, and we will use this same geometry here. The configuration is assumed to be axisymmetric and symmetric across the neutral line down the center of the streamer. There are three regions: R1, R2, and R3, shown here with cross-sectional areas $A_1(r)$, $A_2(r)$, and $A_3(r)$. R1 is the region of closed field lines, the helmet. R2 is adjacent to and below the top of the helmet. Both R1 and R2 extend upward to the height r_h , where the area in R1 goes to zero. R3 is above r_h , the top of the helmet. Area A_{10} is the area of the base of the helmet at $r_0 \geq 1 R_\odot$ and A_{20} is the sum of the open-outflow areas at r_0 on either side of the streamer. The dashed lines marking the outer boundaries of R2 are assumed to be radial so that $A_1(r) + A_2(r) \propto r^2$, and above r_h , $A_3(r) \propto r^2$. An important simplification is achieved by computing only the average values of the physical variables over the cross sections A_1 , A_2 , and A_3 , since this reduces the problem to one dimension. We assume that the plasma in R2 and R3 is isothermal. We also assume that the plasma in R1 is isothermal but with a different temperature than in R2 and R3. This is in keeping with our intention here to focus on the effects of the geometry on flow dynamics and not the energetics of the flow. In § 6 we will discuss relaxing this restriction. Hydrostatic equilibrium is assumed in R1, as is appropriate given the empirical and multidimensional MHD model results that $\beta > 1$ throughout the body of and above the helmet. The base of the model, r_0 , is defined by the height above which $\beta_1 > 1$. Typically, $r_0 = 1.2 R_\odot$ is a conservative choice and $r_0 = 1.0 R_\odot$ is acceptable along a neutral line with no active regions. The physics of this model is that the plasma in the helmet is confined by the pressure from the magnetic field and plasma on adjacent open field lines in R2 pressing on the boundaries of the streamer. This physical interpretation of coronal structure also explains the observed constancy of the radial magnetic field strength in the solar wind when it is mapped to constant radius (Suess & Smith 1996).

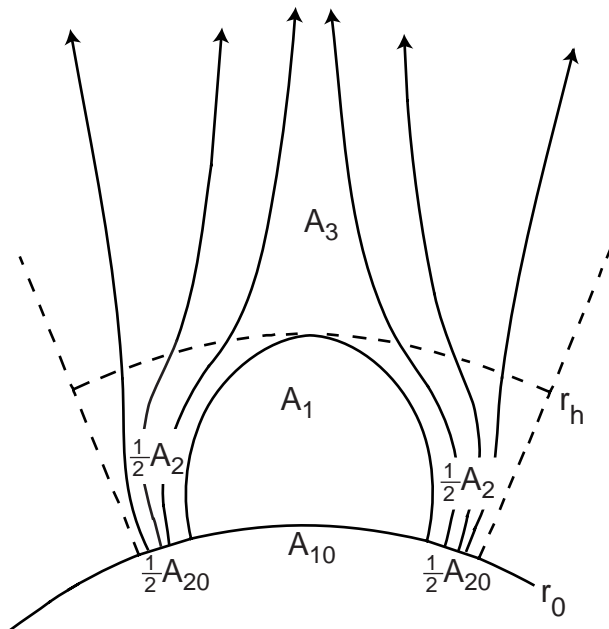


FIG. 3.—Geometry assumed for the streamer model. A_1 , A_2 , and A_3 are described in the text (P68).

The side boundaries of the model, shown by the dashed lines, were interpreted in P68 to lie at the center of coronal holes. Here, we modify this interpretation to be the streamer brightness boundaries. This is based on the results shown in Figure 2, to which we return now. Four magnetic field lines are labeled in Figure 2: B1, B2, C1, and C2. Two of the field lines, C1 and C2, are near the edge of the coronal hole where fields diverge rapidly at these heights. For comparison, the adjacent two field lines, B1 and B2, nearer the center of the coronal hole, are also labeled. It can be seen that B1 and B2 are approximately the same distance apart as other field lines at the same height farther toward the center of the hole. Conversely, C1 and C2 are much farther apart, illustrating the rapid divergence at the edge of the hole. In addition, B1 and B2 are seen to be approximately radial above $1.2 R_\odot$, while C1 and C2 are far from radial. This provides a rationale for our assumption that the boundaries of the model in Figure 3 can be the brightness boundaries, and the flow we model lies in the region labeled A in this figure. To illustrate that this simplification can represent coronal conditions, we note an example of an approximately radial empirical streamer brightness boundary marked as A in Figure 1. Although the restriction to radial brightness boundaries is an important limitation to the model, we will show that the model nevertheless reproduces all important two-dimensional MHD model results. We will also discuss in § 6 how this restriction can be relaxed. We note in passing that the region outside the dashed lines in Figure 3 is coronal hole flow, where it is well known that $\beta \ll 1$.

3. MATHEMATICAL DESCRIPTION OF THE MODEL

To reduce the model to a one-dimensional calculation, we described above the assumption that only the average values of the physical variables over the cross sections A_1 , A_2 , and A_3 will be computed. In this case, the equations describing conditions in Figure 3 are (1) hydrostatic-pressure balance in R1 with mean ion molecular weight μ and base radius (heliocentric distance) r_0 , (2) radial momentum equation for isothermal Parker wind flow with an arbitrary geometric spreading factor in R2, (3) conservation of mass flux in R2 (B_{20} and A_{20} are the magnetic field strength and cross-sectional area at r_0), (5) conservation of total area $A_1(r) + A_2(r)$, (6) pressure balance on the interface between R1 and R2, and (7) in R3 the flow is assumed to be radial. The equations describing the flow in R3 are just the isothermal Parker wind equations. This gives

$$N_1 = N_{10} \exp \left[-\frac{\mu G M_\odot m_p}{r_0 k T_1} \left(1 - \frac{r_0}{r} \right) \right], \quad (1)$$

$$m_p N_2 \left(V_2 \frac{dV_2}{dr} + \frac{G M_\odot}{r^2} \right) = -\frac{k T_2}{\mu} \frac{dN_2}{dr}, \quad (2)$$

$$N_2 V_2 A_2 = N_{20} V_{20} A_{20}, \quad (3)$$

$$B_2 A_2 = B_{20} A_{20}, \quad (4)$$

$$A_1 + A_2 = \frac{r^2}{r_0^2} (A_{10} + A_{20}), \quad (5)$$

$$2k N_1 T_1 = 2k N_2 T_2 + \frac{1}{8\pi} B_2^2, \quad (6)$$

$$m_p N_3 \left(V_3 \frac{dV_3}{dr} + \frac{G M_\odot}{r^2} \right) = - \frac{k T_3}{\mu} \frac{dN_3}{dr}, \quad (7)$$

$$N_3 V_3 A_3 = N_{30} V_{30} A_{30}, \quad (8)$$

$$A_3 = \frac{r^2}{r_h^2} A_{30}, \quad (9)$$

$p_2 = 2N_2 k T_2$, $p_3 = 2N_3 k T_3$, $T_2 = T_3$, and the dimensionless parameters are $\tau = T_1/T_2$ = the temperature ratio, $\Psi = (\mu G M_\odot m_p)/(r_0 k T_1)$, $\mathfrak{R} = A_{20}/A_{10}$ = the area ratio, $\beta_{20} = 2N_{20} k T_2/(B_{20}^2/8\pi)$, and $\eta = N_{10}/N_{20}$ = the density ratio. The subscripts indicate to which region the variables refer. Equation (2) can be integrated and the equations solved analytically, with the requirement that the solution for V_2 pass through the critical point smoothly from subsonic flow close to the Sun to supersonic flow far from the Sun. In practice, the solution is generally found more easily by direct numerical integration of equations (2) and (7) in R2 and R3.

An important parameter in this model is the area ratio, \mathfrak{R} . This is, again, the ratio of the base area in R2, including both sides of the helmet, to the base area in R1. Solutions can be found for a range that is at least as large as $0.01 \leq \mathfrak{R} \leq 100$, depending on the other physical parameters. The ratio $\mathfrak{R} \ll 1$ corresponds to a vanishingly small region R2, while $\mathfrak{R} \gg 1$ corresponds to a vanishingly small helmet and essentially radial flow. The side boundaries to R2 can be anywhere so, guided by an equatorial streamer belt like that depicted in Figure 3, we define the brightness boundary to start at the polar angle ϑ_1 . This is illustrated in Figure 4, where the base of R2 is shown to start at ϑ_1 . The boundary between R1 and R2 is given by the angle $\vartheta(r)$ and $\vartheta(r_0) \equiv \vartheta_0$. Given the transequatorial symmetry of the model, $\vartheta(r_h) = 90^\circ$.

It is easier to work with dimensionless equations so equations (1)–(8) are scaled such that $x = r/r_0$, $m_1 = N_1/N_{10}$, $m_2 = N_2/N_{20}$, $m_3 = N_3/N_{30}$, $u_2 = V_2/(2kT_2/\mu m_p)^{1/2}$, $u_3 = V_3/(2kT_3/\mu m_p)^{1/2}$, $b_2 = B_2/B_{20}$, $y_1 = A_1/A_{10}$, and $y_2 = A_2/A_{20}$. In addition to the above, the dimensionless parameter u_0 appears where $u_0 = V_{20}/[2kT_2/(\mu m_p)]^{1/2}$. The mean molecular weight in terms of the fraction of alpha particles, $\delta \equiv n_\alpha/n_p$ (assuming a plasma of only alpha particles, electrons, and protons), is given by $\mu = (1 + 4\delta)/(2 + 3\delta)$. The

scaled equations are

$$m_1 = \exp \left[-\Psi \left(1 - \frac{1}{x} \right) \right], \quad (10)$$

$$m_2 y_2 u_2 = u_0, \quad (11)$$

$$b_2 y_2 = 1, \quad (12)$$

$$u_2^2 + \ln(m_2) + \tau \Psi \left(1 - \frac{1}{x} \right) = u_0^2, \quad (13)$$

$$y_1 + \mathfrak{R} y_2 = (1 + \mathfrak{R}) x^2, \quad (14)$$

$$\eta \tau m_1 = m_2 + \frac{b_2^2}{\beta_{20}}, \quad (15)$$

$$u_3^2 + \ln(m_3) + \tau \Psi \left(1 - \frac{1}{x} \right) = K_1, \quad (16)$$

$$m_3 u_3 y_3 = K_2, \quad (17)$$

$$y_3 = y_{30} x^2. \quad (18)$$

Note that evaluating equation (15) at $x = 1$ gives $\eta \tau = 1 + 1/\beta_{20}$, which can be used to eliminate η from further appearance in the analysis. The quantity y_1 is a derived quantity that appears only in equation (14). Equations (13) and (16) are the integrated forms of equations (2) and (7). The differential forms are

$$2u_2 \frac{du_2}{dx} + \frac{1}{m_2} \frac{dm_2}{dx} + \Psi \tau \frac{1}{x^2} = 0, \quad (19)$$

$$2u_3 \frac{du_3}{dx} + \frac{1}{m_3} \frac{dm_3}{dx} + \Psi \tau \frac{1}{x^2} = 0. \quad (20)$$

The solution to equations (10)–(18) in the particular case $\tau = 1$ is described in P68. We outline that solution here with the addition of the new analytic expressions for u_0 . In general, the flow begins subsonically at r_0 and becomes supersonic somewhere above r_0 . It was shown in P68 that when the temperatures in R1 and R2 are the same ($\tau = 1$), then the critical point x_c (where the flow becomes supersonic) always lies in R3, and $x_h \leq x_c/2$. The general extension we make to those solutions is to fully relax the restriction that $\tau = 1$. We will begin with cases for which x_c lies in R3 and there is only a single critical point. Other cases will be discussed in § 5.

3.1. Mathematical Solution in R3

The flow in R3 is simple, spherical, isothermal Parker flow for which an analytic solution can be written. This solution has to be matched to the solution in R2. At x_h , the boundary between R2 and R3, the variables must be continuous, which is guaranteed by setting

$$y_2(x_h) = y_3(x_h) \equiv y_h, \quad (21a)$$

$$m_2(x_h) = m_3(x_h) \equiv m_h, \quad (21b)$$

$$u_2(x_h) = u_3(x_h) \equiv u_h. \quad (21c)$$

This immediately gives, from equations (14) and (18), the result that $y_h = (1 + 1/\mathfrak{R})x_h^2$. Next, we look for the critical-point criteria in R3. First, solve equations (16), (17), and (18) for m_h to give

$$m_h = \frac{u_0}{u_h(1 + 1/\mathfrak{R})x_h^2}. \quad (22)$$

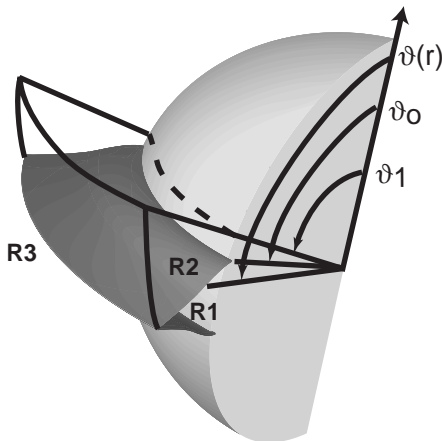


FIG. 4.—Definitions of the angles $\vartheta(r)$, ϑ_0 , and ϑ_1

Substitute this into equation (16):

$$u_3^2 + \ln \left[\frac{K_2}{u_3(1 + 1/\mathfrak{R})x^2} \right] + \Psi\tau \left(1 - \frac{1}{x} \right) = K_1. \quad (23)$$

Eliminating K_2 and evaluating at x_h ,

$$u_3^2 + \ln \left(\frac{m_h u_h x_h^2}{u_3 x^2} \right) + \Psi\tau \left(1 - \frac{1}{x} \right) = K_1 \\ = u_h^2 + \ln(m_h) + f_h \tau, \quad (24)$$

where

$$f \equiv \Psi \left(1 - \frac{1}{x} \right), \quad (25)$$

$$f_h = \Psi \left(1 - \frac{1}{x_h} \right). \quad (26)$$

Equation (24) simplifies to

$$u_3^2 - \frac{1}{2} \ln(u_3^2) = \ln \left(\frac{x^2}{x_h^2} \right) - \frac{1}{2} \ln(u_h^2) + u_h^2 + \Psi\tau \left(\frac{1}{x} - \frac{1}{x_h} \right). \quad (27)$$

The derivative of equation (27) gives the equation defining the critical points:

$$\frac{du_3}{dx} \left(2u_3 - \frac{1}{u_3} \right) = \frac{1}{x} \left(2 - \frac{\Psi\tau}{x} \right). \quad (28)$$

The right-hand side of equation (28) goes through zero at the critical point where

$$x_{3c} = \frac{\Psi\tau}{2}. \quad (29)$$

At the critical point the left-hand side must also be zero. This can happen by either the velocity going through an extremum ($du_3/dx = 0$) or the quantity in the brackets going through zero. The solution in R3 is monotonic (Parker 1963), so the latter must be the case, and at x_{3c} ,

$$u_{3c}^2 = \frac{1}{2}. \quad (30)$$

Equations (29) and (30) describe the critical-point conditions in R3 so long as $x_{3c} > x_h$. From equation (29), x_{3c} depends only on r_0 and μ/T_2 . The physical statement of this is that there will be a critical point in R3 as long as the flow is not already supersonic when it enters R3 at x_h . Equation (27) can now be evaluated at x_{3c} to give the relationship between u_h and x_h :

$$2u_h^2 - \ln(u_h^2) = 2 \frac{\Psi\tau}{x_h} - 3 + \ln \left[32 \left(\frac{x_h}{\Psi\tau} \right)^4 \right]. \quad (31)$$

3.2. Mathematical Solution in R2

Equations (11) and (13) combine to eliminate m_2 and give

$$y_2 = \frac{u_0}{u_2} \exp \left[u_2^2 - u_0^2 + \Psi\tau \left(1 - \frac{1}{x} \right) \right]. \quad (32)$$

At $x = x_h$, the area in R1 goes to zero, so that from equation (14),

$$y_2(x_h) \equiv y_h = \left(1 + \frac{1}{\mathfrak{R}} \right) x_h^2. \quad (33)$$

Using equations (32) and (33) at x_h gives

$$\left(1 + \frac{1}{\mathfrak{R}} \right) x_h^2 = \frac{u_0}{u_h} \exp \left[u_h^2 - u_0^2 + \Psi\tau \left(1 - \frac{1}{x_h} \right) \right]. \quad (34)$$

This equation can be manipulated to derive an equation for u_0 that depends only on the physical parameters, not on any of the other derived parameters, and satisfies the requirements for continuity with the solution in R3. Begin by taking the logarithm of equation (34) to give

$$u_h^2 - u_0^2 + \Psi\tau \left(1 - \frac{1}{x_h} \right) = \ln \left[\frac{u_h}{u_0} x_h^2 \left(1 + \frac{1}{\mathfrak{R}} \right) \right]. \quad (35)$$

To make this more compact, use the notation

$$z_h \equiv \frac{x_h}{\Psi\tau}, \quad (36a)$$

$$\lambda \equiv \Psi^2 \tau^2 \left(1 + \frac{1}{\mathfrak{R}} \right). \quad (36b)$$

Using these in equation (35) and combining that with equation (31) gives

$$u_0^2 - \ln(u_0) = \Psi\tau - \frac{3}{2} + \frac{5}{2} \ln(2) - \ln(\lambda) \equiv C, \quad (37)$$

where the constant, C , depends only on the physical parameters of the problem, including the area ratio, \mathfrak{R} . Equation (37) is a new equation that was not obtained in P68. It is a transcendental equation for only u_0 that depends on the solution in R3, because equation (31) was used in its derivation. Thus, it is the solution for u_0 , the velocity at the base of the model, which is required for the solution to pass smoothly from subsonic flow at the base to supersonic flow far from the Sun when the critical point is in R3. Generally, equation (37) has two real roots corresponding to subsonic and supersonic injection of plasma at the base of the corona. We focus on the subsonic root.

The equation for u_2 is derived by eliminating m_2 by using equation (13) in equation (15) to give

$$1 + \frac{1}{\beta_{20}} = \exp \left[u_0^2 - u_2^2 + \Psi \left(1 - \frac{1}{x} \right) (1 - \tau) \right] \\ + \frac{1}{\beta_{20}} \frac{u_2^2}{u_0^2} \exp \left[2(u_0^2 - u_2^2) + \Psi \left(1 - \frac{1}{x} \right) (1 - 2\tau) \right], \quad (38)$$

which is equation (14) in P68. When equation (38) is differentiated it gives

$$\frac{du_2}{dx} \left\{ u_0^2 \exp \left[u_2^2 - u_0^2 + \Psi\tau \left(1 - \frac{1}{x} \right) \right] - \frac{1}{\beta_{20}} (1 - 2u_2^2) \right\} \\ = \frac{\Psi}{2u_2 x^2} \left\{ \frac{u_2^2}{\beta_{20}} (1 - 2\tau) - u_0^2 (\tau - 1) \right. \\ \left. \times \exp \left[u_2^2 - u_0^2 + \Psi\tau \left(1 - \frac{1}{x} \right) \right] \right\}. \quad (39)$$

The physical solution is found by numerically integrating the differential forms of the equations (19) and (20) rather than solving the transcendental integrated equations for the appropriate roots. The height of the helmet, x_h , is determined when $y_1 \rightarrow 0$. By directly solving for the continuous solution from subsonic flow at the base to supersonic flow

far from the Sun, we have bypassed alternative solution branches. The solution space for these equations is analogous to the solution space for the original Parker equations, with the potential for additional complexity because of the non- r^2 geometric expansion in R2 (Kopp & Holzer 1976; Leer & Holzer 1990).

The derivation here is simple and concise. However, we have avoided spending time dealing with many real complexities that were discussed in P68. Our goal is instead to go directly to illustrating two important extensions to the results in P68. The first is that the solutions shown above are for $\tau \neq 1$, a major generalization to P68 that allows us to examine a much larger class of flow regimes than could be achieved by the $\tau = 1$ restriction. The second is an extension to the specific results described in P68 for which an upper bound to the permissible temperature in streamers was derived. We turn to this second extension now.

3.3. Mathematical Solution for $\tau = 1$

The $\tau = 1$ solutions were extensively discussed in P68, and we only summarize some of the results here. First, equation (39) reduces to equation (16) in P68 in the limit $\tau = 1$; i.e.,

$$\frac{du_2}{dx} \left\{ u_0^2 \exp \left[u_2^2 - u_0^2 + \Psi \tau \left(1 - \frac{1}{x} \right) \right] - \frac{1}{\beta_{20}} (1 - 2u_2^2) \right\} = - \frac{\Psi u_2}{2x^2 \beta_{20}}. \quad (40)$$

First, note that $u_2^2 = \frac{1}{2}$ corresponds to the flow velocity being the speed of sound, the same as equation (30) in R3. If $u_2^2 = \frac{1}{2}$, the left-hand side of equation (40) is positive. The right-hand side, however, is always negative. Therefore, the equation can be satisfied only if du_2/dx is negative. So, the $\tau = 1$ case exhibits only one critical point that must lie in R3. We seek solutions for which the speed increases from low values near r_0 to supersonic flow in R3. Therefore, the flow adjacent to the helmet is subsonic, the critical point lies in R3 when $\tau = 1$, and the assumption implicit in § 3.1 is valid.

It was also shown in P68 that in this case $x_h \leq \Psi/4$, so the maximum possible extension of the closed magnetic field helmet region is one-half the distance to the critical point in R3. This occurs for a specific temperature, $T_{1,\max}(\mathfrak{R}_{\max}, \Psi_{\min})$, and it was shown that at this temperature

$$\frac{1}{2} \Psi_{\min} - 2 \ln \Psi_{\min} = \ln(1 + 1/\mathfrak{R}_{\max}) + 2 - 4 \ln 2, \quad (41)$$

where it is to be noted that Ψ_{\min} is a minimum because $\Psi \propto 1/T_1$.

In P68 this was interpreted as the maximum temperature above which the streamer cannot exist with an internal helmet of closed hydrostatic plasma. The temperature was so high that the gas was simply too hot to be held stationary by the surrounding pinch of the magnetic field in R2. This interpretation, however, did not take into account the point that \mathfrak{R} is a physical parameter that might also be expected to vary as T increases. This is addressed below.

3.4. Solution Isomorphism

Nondimensional solutions can be used to generate many dimensional solutions, but there is also an interesting isomorphism that can be used to generate many solutions from one nondimensional solution. To show this, fix Ψ , β_{20} , and

u_0 , the subsonic root from equation (37), all for a given r_0 . Because Ψ depends only on the ratio μ/T_1 , changing μ or T_1 while keeping the ratio constant allows the generation of other solutions without solving the nondimensional equations again. Further, u_0 depends only on \mathfrak{R} and μ/T_2 . Equation (37) shows that for a fixed value of u_0 and a specified value of μ/T_2 ($\Psi\tau = \text{constant}$), \mathfrak{R} can be calculated such that u_0 does not change. Finally, a fixed value of β_{20} implies that $N_{20} T_2/B_{20}^2$ does not change. Choosing N_{20}/B_{20}^2 allows the calculation of T_2 so that β_{20} is constant. This determines μ (because μ/T_2 is known), which in turn determines T_1 from Ψ and μ . We have thus generated a new solution with different \mathfrak{R} , μ , T_2 , and T_1 from the original nondimensional solution. Aside from comparing our results with the original calculation in P68, which used $\mu = 0.69$, we have little interest in generating new solutions with different values of μ . Therefore, keeping μ equal to, e.g., 0.56, the isomorphism is used by specifying T_2 and then calculating \mathfrak{R} such that u_0 is unchanged. Then the value of N_{20}/B_{20}^2 is calculated from both T_2 and the original value of β_{20} . Finally, T_1 remains unchanged from the original solution. This can be summarized by

$$\Psi = \Psi(\mu/T_1), \quad (42a)$$

$$u_0 = u_0(\mathfrak{R}, \mu/T_2), \quad (42b)$$

$$\beta_{20} = \beta_{20}(N_{20} T_2/B_{20}^2). \quad (42c)$$

We illustrate the use of this isomorphism by using the P68 solution with $\mu = 0.69$ and generating the new solution with $\mu = 0.56$. (Eq. [6], the pressure-balance condition, was missing a factor of 2 in P68.) The parameters in P68 are $N_{20} = 2 \times 10^8 \text{ cm}^{-3}$, $T_1 = T_2 = 1.5 \times 10^6 \text{ K}$, and $B_{20} = 0.5\text{--}2 \text{ G}$. We take $B_{20} = 2 \text{ G}$. Then T_1 and $T_2 = 1.22 \times 10^6 \text{ K}$, which is decreased by the ratio of $\mu_{\text{new}}/\mu_{\text{old}}$. Because μ_{old} is the same value as in P68, equation (42b) requires the same value of \mathfrak{R} (unspecified). Then $B_{20} = 1.80 \text{ G}$, so that β_{20} is still 0.52. Only $T_1 = T_2$ and B_{20} change. The nondimensional solution of equations (10)–(18) remains the same, but dimensional solutions change through the scaling ratios.

3.5. Character of the Solution Space

The general solution space can be plotted for three of the four variables, T_1 , T_2 , \mathfrak{R} , and β_{20} , for fixed $\mu = 0.56$ and r_0 , that determine the solution. We have chosen to fix β_{20} and plot the solution of equation (38) evaluated at x_h . We neglect $|u_0^2 - u_h^2|$ compared to u_{3c}^2 so that equation (38) may be written as

$$\frac{u_h^2}{u_0^2} = (1 + \beta_{20}) \exp [f(2\tau - 1)] - \beta_{20} \exp (f\tau). \quad (43)$$

This is the new version of equation (25) in P68. Now equation (34) may be used to eliminate u_h^2/u_0^2 from equation (38), giving

$$\frac{u_h}{u_0} \left(1 + \frac{1}{R} \right) x_h^2 = \exp (\tau f_h), \quad (44)$$

so

$$(1 + \beta_{20}) \exp [f(\tau - 1)] - \beta_{20} = \frac{\exp (f\tau)}{[x_h^4(1 + 1/R)^2]}. \quad (45)$$

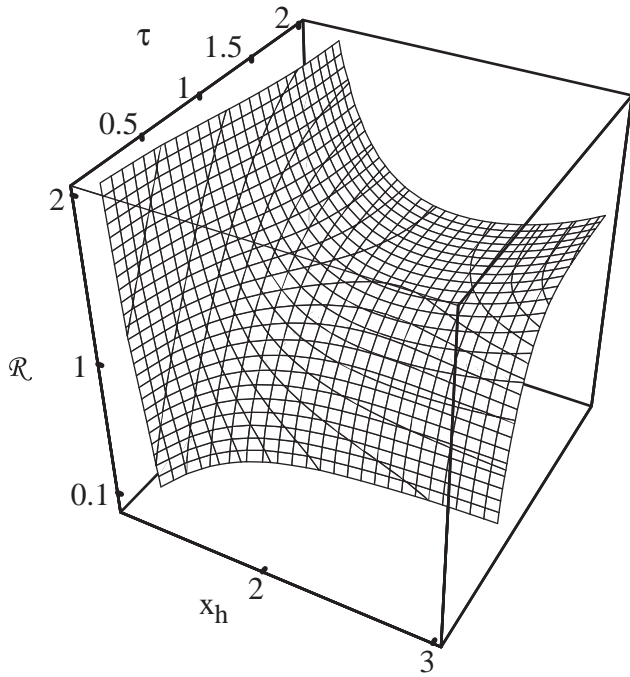


FIG. 5.—Solution space from eq. (45) for $\mu = 0.56$ and $T_1 = 1.5 \times 10^6$ K. In this plot the τ -axis corresponds to varying T_2 , since T_1 is held fixed. The helmet height, x_h , is plotted vs. $\mathfrak{R} = A_{20}/A_{10}$ and τ . Each contour on the surface is for a constant \mathfrak{R} , constant τ , or constant x_h , the non-dimensional helmet height. Helmets with $x_h \gtrsim 1.5 R_\odot$ require $\mathfrak{R} \sim 1$ when $\tau = T_1/T_2 > 0.5$. The solution assumes $|u_0^2 - u_h^2| \ll u_{3c}^2$.

Figure 5 is a plot of the solution to equation (45) when $\beta_{20} = 0.26$ and $T_1 = 1.5 \times 10^6$ K, where it should be remembered that although the plot for a varying $\tau = T_1/T_2$, only T_2 is actually varying. The saddle surface shows that

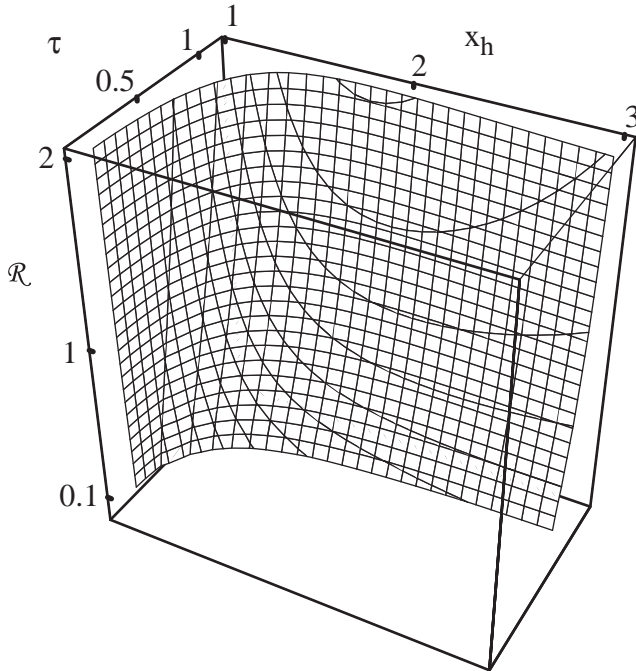


FIG. 6.—Solution space from eq. (45) for $\mu = 0.56$ and $T_2 = 1.5 \times 10^6$ K. Opposite to Fig. 5, the τ -axis now corresponds to varying T_1 , since T_2 is held fixed. The streamer height, x_h , is plotted vs. $\mathfrak{R} = A_{20}/A_{10}$ and τ . Helmets with $x_h \gtrsim 1.5 R_\odot$ only exist for $\tau \sim 1$. There is little variation in the solution space for varying \mathfrak{R} . The solution assumes $|u_0^2 - u_h^2| \ll u_{3c}^2$.

the solution space is constrained to approximately $\tau > 0.5$ for tall helmets to exist ($x_h > 1.5$). Tall helmets also require $\mathfrak{R} \sim 1$. As we move down the saddle, tall helmets exist only for small \mathfrak{R} , so that these helmets are both tall and wide. Values of $\mathfrak{R} > 1.5$ generally produce short helmets, indicating that these helmets are both narrow and short.

Figure 6 shows the solution space when $T_2 = 1.5 \times 10^6$ K and T_1 is allowed to vary. Clearly, tall helmets require a narrow range for T_1 where $\tau \sim 1$. Similar solution-space plots (not shown) for $T_2 = 1.3 \times 10^6$, 1.7×10^6 , and 1.8×10^6 K indicate that the upper bound for τ decreases from $\lesssim 1.2$ to less than 1 as T_2 increases to 1.8×10^6 . We also examined the solution space for $10 > \beta_{20} > 0.01$, $T_2 = 1.5 \times 10^6$ K, and $\mathfrak{R} = 0.5$, and found the same requirement that $\tau \sim 1$ for helmets higher than $\sim 1.5 R_\odot$, and no tall helmets at all for $\tau \lesssim 0.6$ no matter what the value of \mathfrak{R} .

4. PHYSICAL SOLUTIONS

To illustrate solutions to equations (1)–(9), we begin by defining a set of physical parameters. We start with \mathcal{G}_1 from Figure 4, the angular half-width of the streamer base at r_0 . Here we uniformly take $\mathcal{G}_1 = 70^\circ$. If we consider a quiet streamer, we can select $r_0 = 6.96 \times 10^{10}$ cm, $B_{20} = 2.0$ G, and $N_{20} = 10^8$ cm $^{-3}$. Given \mathcal{G}_1 and these conditions, we can compute $A_1(r)$ in terms of $\mathcal{G}(r)$ for different values of T_1 and T_2 . Consider first the simple case described in § 3.3, $\tau = 1$. We also initially use $\mu = 0.69$ (17% alpha particles) to compare with P68, who also used that value, although a better choice for the solar wind that we will use below is $\mu = 0.56$ (5% alpha particles; Aellig, Lazarus, & Steinberg 2001).

4.1. $\tau = 1$

Figure 7a shows the variation of $A_1(r)$ with height for a series of $\tau = 1$ solutions. The solutions are for a range in T_1 when $\mathfrak{R} = 0.5$. For visualization, what is actually shown is a polar plot of $\mathcal{G}(r)$ from Figure 4, computed as follows:

$$y_1(r) \equiv A_1(r)/A_{10}, \quad (46a)$$

$$y_2(r) \equiv A_2(r)/A_{20}, \quad (46b)$$

$$\mathcal{G}(r) = \arccos \{ \cos \mathcal{G}_1 / [1 + \mathfrak{R} y_2(r)/y_1(r)] \}. \quad (46c)$$

The helmet shapes are domed for lower temperatures and become sharply cusped at higher temperatures. Moreover, there is the interesting property noted in P68 that there is no solution for $T_1 > 1.62 \times 10^6$ K for $\mathfrak{R} = 0.5$. As we have noted elsewhere (Suess & Nerney 1999), this does not necessarily imply a lack of solution, but rather that the streamer begins to shrink in cross section at the base at higher temperatures. This shrinkage corresponds to an increase in \mathfrak{R} , and at some finite temperature it is found that the helmet completely disappears, while at the same time, $x_h \rightarrow 1$. This is illustrated in Figure 7b. Finally, above a temperature of about 3.5×10^6 K, there truly is no solution. This interpretation extends the results in P68 to give the complete evolutionary track of a helmet under increasing temperature, from a broad helmet of zero height for low temperatures to a maximal-height helmet for $T_1 \sim 1.62 \times 10^6$ K to a helmet of zero height and width at $T \sim 3.5 \times 10^6$ K. The evolutionary track is shown in Figure 8, starting with a fixed-area ratio and then increasing the area ratio once the maximum temperature is reached for the initial value of \mathfrak{R} . However, this is a rather limited

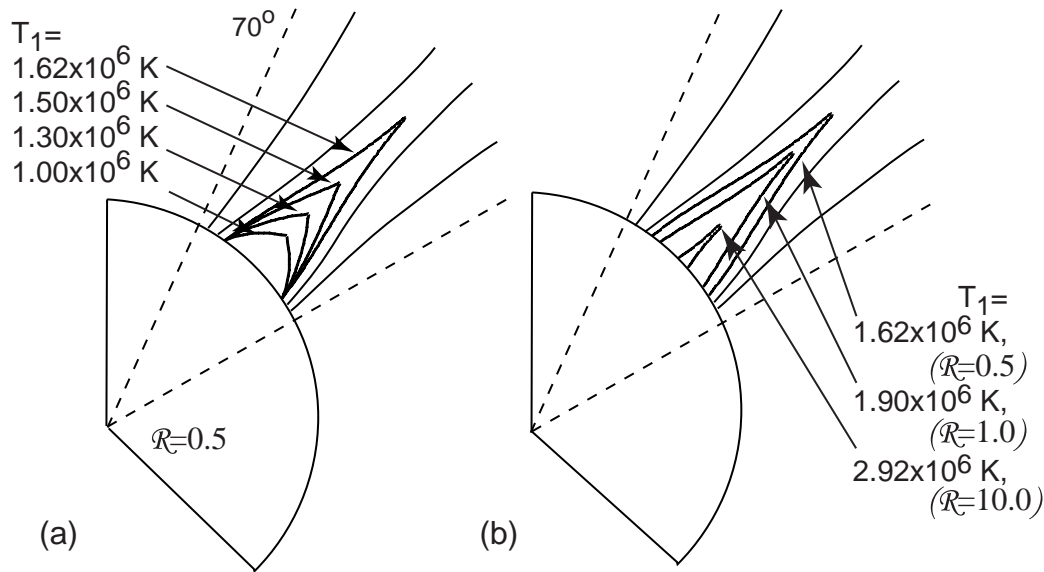


FIG. 7.—(a) Variation of helmet shape $[A_1(r)]$ as a function of temperature T_1 for a fixed-area ratio $\mathfrak{R} = 0.5$ for temperatures up to the maximum value for $\mathfrak{R} = 0.5$, $T_1 = 1.62 \times 10^6$ K. (b) Variation of helmet shape as a function of temperature for $T_1 > 1.62 \times 10^6$ K. The other physical parameters for this example are $B_{20} = 2.0$ G, $N_{20} = 10^8 \text{ cm}^{-3}$.

example because $\tau = 1$. In § 4.2 we will tabulate maximum temperatures and heights for a broader range of cases.

As we have shown elsewhere (Suess et al. 1999b), any polytropic solar wind model with a volumetric heat source will have monotonically increasing temperature in the helmet because there is no mechanism for removing the energy input in the absence of an outflow. If the temperature increase is slow enough so the temperature increase is slow compared to the characteristic times for the transit of sound and fast mode waves through R1 and R2 in Figure 3, then the evolutionary track shown in Figure 8 reproduces the phenomenon we have called streamer evaporation.

Figure 9 shows the flow speed, spreading factor, and number density for the solutions in Figure 7a. The curves are labeled by their temperatures, corresponding to the four helmet-shape solutions. The spreading factor, $f(r)$, is defined

by

$$A_2(r) = A_{20} \frac{r^2}{r_0^2} f(r) |_{r_0 \leq r \leq r_h}, \quad (47a)$$

$$f(r) |_{r \geq r_h} = \frac{A_{30}}{A_{20}} f(r_h). \quad (47b)$$

The flow speed in Figure 9 increases monotonically and continuously from the base out past the critical point, r_{3c} , in R3, where the flow becomes supersonic. As described in § 3.1, there is only one critical point when $\tau = 1$, and it always lies in R3. There is a discontinuity in the slope of both the flow speed and the number density at r_h that is not easily visible here but which will become more apparent in the solutions shown below for $\tau \neq 1$. Also plotted is the flow speed for $\mu = 0.56$ to show that it is important in these Parker-type solutions to select a realistic value for the amount of helium present. Changing from $\mu = 0.69$, corresponding to 17% helium, to $\mu = 0.56$ results in an approximate factor of 2 increase in the flow speed at $2.0 R_\odot$.

The spreading factor in Figure 9 increases up to r_h and is constant above r_h because of the assumption that $A_3(r) \propto r^2$. The discontinuity in slope for $f(r)$ is the reason there is a discontinuity in slope for the flow speed and density. The four cases illustrated here all have $\mathfrak{R} = 0.5$, so the value of $f(r)$ in R3 is the same for each case. The number density in Figure 9 has the same starting value in each case. Therefore, as T increases, the flow speed at the base, u_0 , increases monotonically and the mass flux correspondingly increases. Thus, the density at any given height also increases monotonically with temperature.

Finally, a peculiarity of these solutions, dependent on the fact that $\tau = 1$, is that they are independent of the value of B_{20} . This is because N_{10} , which is effectively a dependent variable, changes with B_{20} through equation (6) to maintain the same shape for the helmet under changing B_{20} . This property of the model is a consequence of the restriction to a radial brightness boundary, and ways to relax the limitation will be discussed further in § 6.

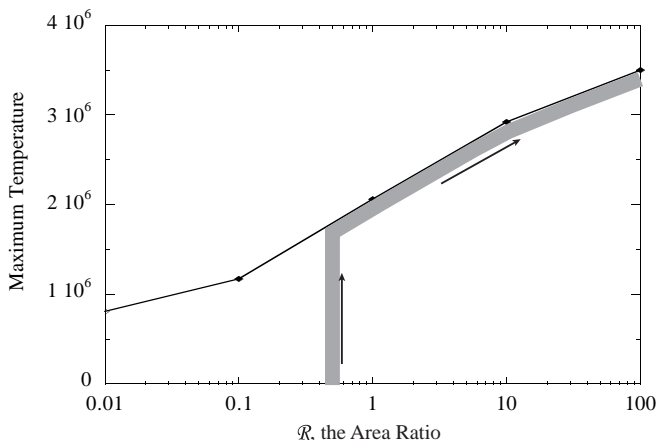


FIG. 8.—Maximum temperature for given area ratio, \mathfrak{R} , and for $\tau = 1$, above which no closed helmet solution exists. The gray evolutionary track is described in the text.

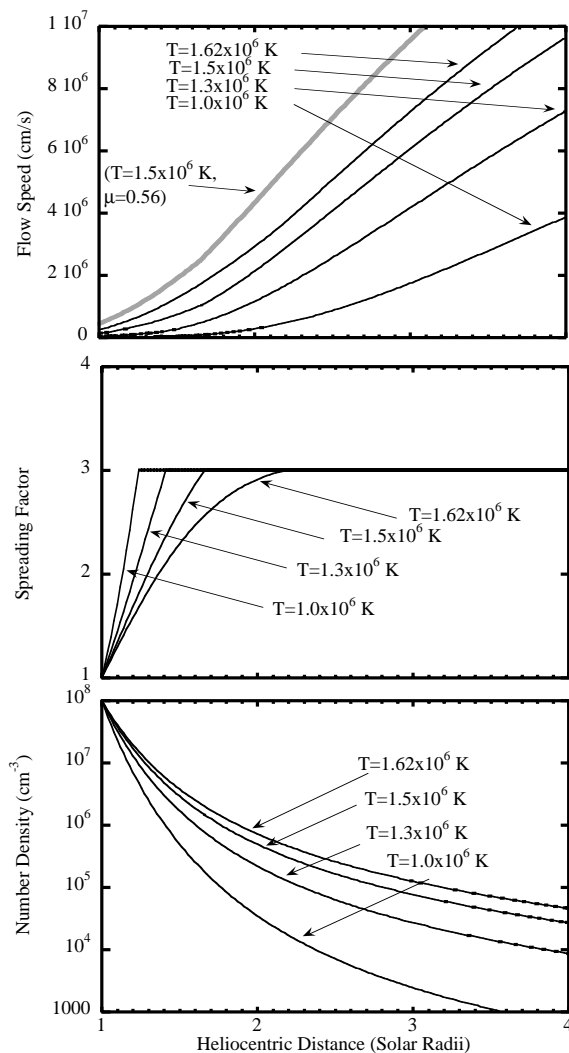


FIG. 9.—Flow speed, spreading factor, and number density for the four solutions shown in Fig. 7a. $\tau = 1$, so the temperatures are for R1 as well as R2 and R3. The other parameters are listed in the text and $\mu = 0.69$. Also shown is the flow speed for $\mu = 0.56$, $T = 1.5 \times 10^6$ K.

These solutions serve to introduce the general properties of solutions to equations (1)–(9), including the following: (1) Helmet shapes like those found both numerically and empirically are reproduced by this simple model. (2) The predicted heights of helmets are similar to those predicted in numerical studies. (3) The behavior of the helmet geometry under changing temperature is similar to that in numerical studies (Steinolfson et al. 1982).

4.2. $\tau \neq 1$ and Stagnation Flow at the Cusp

The results in § 4.1 are limited by the restriction to $\tau = 1$, irrespective of the assumption of an isothermal gas in R1 and R2. Here we relax this restriction and derive an interesting stagnation flow at the cusp. The mathematics for $\tau \neq 1$ has been shown above. The full set of parameters, even for the simple physical example described here, is the set R , T_1 , T_2 , N_{20} , B_{20} , and r_0 . It is impossible to show a full survey of parameter space, and we show instead two sets of three solutions, each of which illustrate many of the interesting features. The first set is for varying T_1 and the second is for varying T_2 ; all other parameters are held constant,

TABLE 2

TEMPERATURES FOR SOLUTIONS A–E

Case	T_1	T_2
A	1.1×10^6 K	2.1×10^6 K
B	1.3×10^6 K	2.1×10^6 K
C	1.5×10^6 K	2.1×10^6 K
D	1.1×10^6 K	1.7×10^6 K
E	1.1×10^6 K	1.3×10^6 K

NOTE.—Temperatures used for computing solutions A–E that are discussed in the text and illustrated in Figs. 10–13.

with $\Re = 0.4$, $r_0 = 1 R_\odot$, $\mu = 0.56$, and $N_{20} = 1.25 \times 10^8 \text{ cm}^{-3}$. The values of T_1 for the first set of three examples are cases A, B, and C in Table 2, while the values of T_2 for the second set of three examples are cases C, D, and E in Table 2. Note that the two sets share case C.

Figure 10 shows a set of solutions for cases A, B, and C in which T_1 varies. Because T_2 and \Re are the same for all these cases, the flow in R3 does not change and the velocity profiles all converge to various points on the same R3 profile at their individual values of r_h . The critical point in R3 for all three solutions is marked by the diamond at $3.077 R_\odot$. The helmet shapes are all more domed than the examples shown in Figure 7, and this is seen to have an immediate consequence in the velocity profile. All three examples exhibit a maximum in flow speed below the top of the helmet. This is

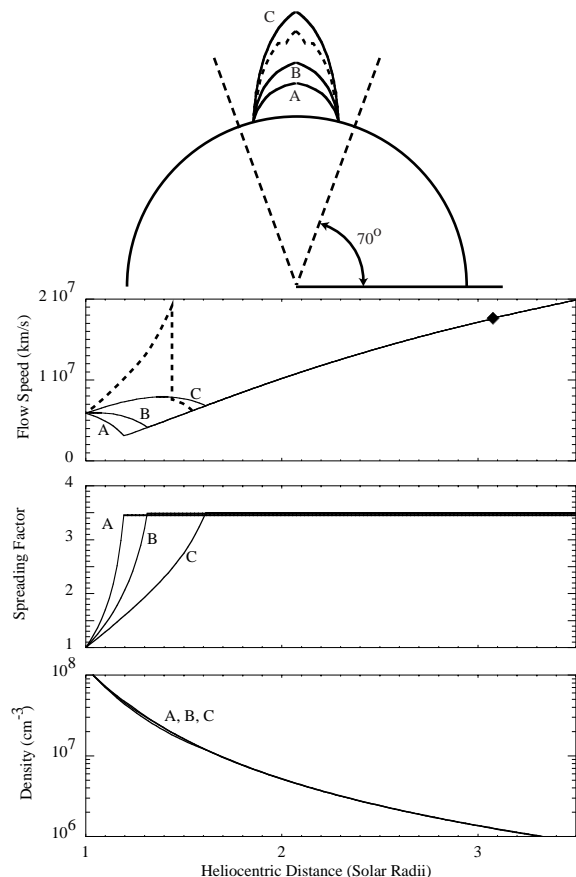


FIG. 10.—Helmet shapes, flow speeds, spreading factors, and number densities for the three cases A, B, and C from Table 2 and discussed in the text. The filled diamond in the flow-speed panel shows the location of the critical point in R3 for all three cases.

a type of stagnation flow that has been found earlier in a two-dimensional MHD simulation by Vázquez et al. (1999). Here, we recover the local peak in speed below the helmet top in this much simpler one-dimensional simulation. These three examples all have the same T_2 and \mathfrak{R} , so the flow speed u_0 is also the same in A, B, and C. The only thing that is changing the flow in R2 is the changing shape of the helmet in response to the changing pressure inside R1 as T_1 is varied. Since \mathfrak{R} does not change, the width of the helmet is unchanging and the value of the spreading factor, $f(r)$, is the same in R3 for these three examples. The density changes little between the three examples. This is because the flow speed is quite small in R2, maximizing at about 75 km s^{-1} in C, so the density is primarily determined by the gravitational scale height. The physics of the local velocity peak in R2 is that the rapid increase in $f(r)$ causes deceleration of the subsonic flow, just as occurs for subsonic flow in a rocket nozzle. The field lines diverge so rapidly in these three examples that the velocity begins to decrease, eventually converging to the velocity profile for R3. The maximum value of $f(r) = f(r_h)$ is determined from

$$\mathfrak{R} = A_{20}/A_{10}, \quad (48a)$$

$$f(r_h) = A_{20} + A_{10} \quad (48b)$$

$$= 1 + 1/\mathfrak{R}. \quad (48c)$$

Therefore, in all three cases A, B, and C, $f(r_h) = 3.5$. The interaction between $f(r)$ and the velocity profile varies, however, depending on the magnitude of the velocity where $f(r)$ is most rapidly changing, moving the peak speed in R2 from the base in A outward to $1.4 R_\odot$ in C.

Solution C in Figure 10 is roughly that for the maximum temperature that can be attained using the one-dimensional model, which in this case is not the maximum temperature described in connection with Figure 8. The reason for the maximum here is suggested by the dashed lines in the flow-speed and helmet-shape panels. When $T_1 > 1.5 \times 10^6 \text{ K}$, the flow becomes supersonic in R2. When this happens, there must be a shock in the velocity profile in R2 to match smoothly with the flow in R3. We schematically show this phenomenon here because it is easiest to understand for the case of constant T_2 . As the flow accelerates around the helmet there is always the possibility that it becomes supersonic. When this happens, flow information from beyond the critical point in R2 can no longer reach r_0 . In this case, a standing shock must occur somewhere in R2, and the location of the shock is determined by the jump conditions leading to a flow profile that matches onto the flow in R3. This is similar to the procedure described in the case of multiple critical-point solutions by Kopp & Holzer (1976). We could solve for these solutions but they introduce a phenomenon that is probably not physically realistic. The pressure undergoes a discontinuous increase with increasing radius at the shock that, by equation (6), means the $A_1(r)$ and $A_2(r)$ must also undergo discontinuous changes in the way suggested by the dashed shape in the top panel of Figure 10. This discontinuity in the area almost certainly would not be realized physically in such a dramatic way. Instead, there would probably be a discontinuous change in the inclination of the helmet boundary at the location of a standing shock. We discuss this phenomenon further in § 6.

Figure 11 shows the set of solutions for cases A, D, and E in Table 2 that have varying T_2 while T_1 and \mathfrak{R} are held

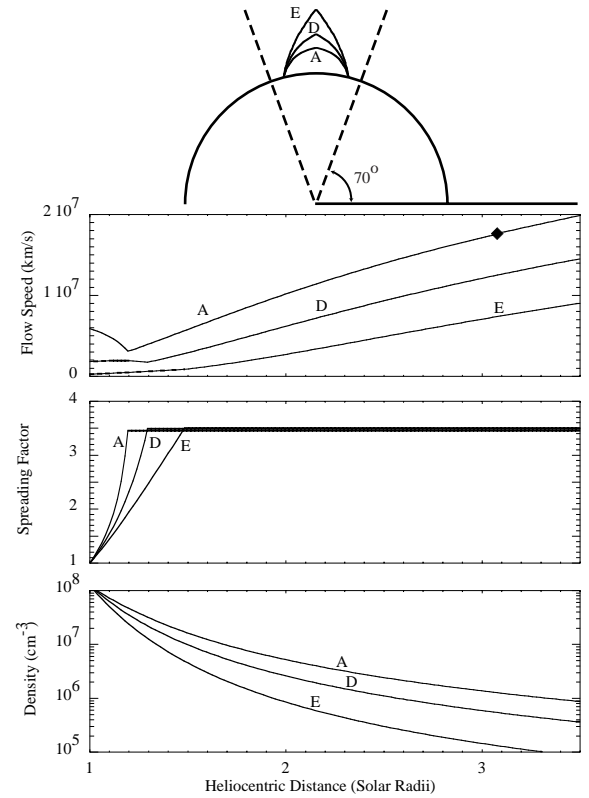


FIG. 11.—Helmet shapes, flow speeds, spreading factors, and number densities for the three cases A, D, and E from Table 2 and discussed in the text.

constant. Case A is the same as A in Figure 10, so we have retained the same label. Here the well-known dependence of u_0 on T_2 in polytropic and isothermal wind models is clearly exhibited. Also, these solutions have different profiles in R3. The critical point for A is shown by the diamond. The critical points for D and E are beyond $3.5 R_\odot$. In these examples, the helmet is slightly more domed than the examples in Figure 10. The consequence is that we have not been able to follow these solutions to as large of values for r_h as for those in Figure 10. For $T_2 > 2.1 \times 10^6 \text{ K}$ the flow again becomes supersonic in R2 and a standing shock forms, so we have ended the series of solutions with example E. The spreading functions for these three examples again all maximize at $f(r_h) = 3.5$ because $\mathfrak{R} = 0.4$. The gradients in $f(r)$ are slightly larger inside r_h than in A, B, and C as a consequence of the more domed shape of the helmets. The density profiles show a larger spread here because the temperature in R3 is changing.

Figure 11 shows that the stagnation flow around the streamer is most prominent when there are large flow speeds at low heights in R2. The solutions are closely coupled to the shape of the streamer, however, which is responding to the changing ambient density near r_h . Since these solutions are for constant N_{20} , decreasing T_2 and u_0 results in lowering the density everywhere in R2 and therefore in raising r_h .

Before leaving this section, we briefly note that all of the solutions shown here have values for $r_h < 2.0 R_\odot$. There is no case in which we have been able to find $r_h > 3.0 R_\odot$ in the absence of a standing shock. Figures 5 and 6 suggest

such solutions may exist in theory but apparently this is for parameters far from typical for the solar corona. This has interesting implications for the Sun. Numerical simulations seem to indicate that the helmet can sometimes extend above $3.0 R_{\odot}$, but these may be numerical artifacts and we trust the general results from this quasi-analytic model for this purpose. The observation that streamers extend much higher than this merely emphasizes that the closed helmet extends only partway up the streamer, and it would be a mistake to equate the two. Therefore, we conclude that the helmet is normally only a small part of the streamer, and that outflow is the most common state in the field of view of the Large Angle and Spectrometric Coronagraph Experiment (LASCO/C2) above $2.0 R_{\odot}$.

4.3. β

We have made the assumption that $\beta > 1$ in R1, and it is possible to consider the self-consistency of this assumption. There is no explicit magnetic field in R1, so it is impossible to strictly evaluate the self-consistency. Instead, we need to make an estimate for the magnitude of B_{10} and B_1 . To begin, take $B_1 = 0.55$ G at $1.15 R_{\odot}$ from the case analyzed by Li et al. (1998). With this choice, we find $\beta > 3$ for all the examples shown in Table 2, where $N_1(r)$, derived from equation (6), ranges from 1.3×10^8 to $1.7 \times 10^8 \text{ cm}^{-3}$ at this height. These densities are all slightly larger than the density quoted by Li et al. at $1.15 R_{\odot}$, but by no more than 50%. If, instead, we take $B_{10} = 2$ G at $r_0 = 1 R_{\odot}$, the same as B_{20} , we find $\beta = 1.3$ – 1.4 at the base of R1, where N_{10} ranges between 5.6×10^8 and $7.6 \times 10^8 \text{ cm}^{-3}$. The model results illustrated in Figure 2 and discussed in Suess et al. (1999a) indicate β is always above this base value in the helmet, so these base values are also minimum values. The results for the base values are tabulated in Table 3. If we increase B_{10} to 4 G, perhaps a more realistic value given recent empirical results, and redo the calculations for case E, then $\beta_{10} = 1.1$, still preserving the validity of our assumption. From these numbers, we conclude that $\beta > 1$ in R1 is a physically reasonable assumption that is self-consistent with this one-dimensional model and the examples shown here.

Turning to the other regions shown in Figure 2, no explicit assumption has been made for β in R2 or R3. We

TABLE 3
PLASMA β IN R1

Case	Density	β
1.0 R_{\odot} , 2.0 G		
A	$7.6 \times 10^8 \text{ cm}^{-3}$	1.5
D	$7.2 \times 10^8 \text{ cm}^{-3}$	1.4
E	$6.7 \times 10^8 \text{ cm}^{-3}$	1.3
1.15 R_{\odot} , 0.55 G		
A	$1.5 \times 10^8 \text{ cm}^{-3}$	3.8
D	$1.4 \times 10^8 \text{ cm}^{-3}$	3.6
E	$1.3 \times 10^8 \text{ cm}^{-3}$	3.4

NOTE.—Plasma β in R1 at the base and at $1.15 R_{\odot}$. The field strength at the base is chosen to be the same as B_{20} , while that at $1.15 R_{\odot}$ is the same as used in Li et al. 1998. The temperature in R1 is 1.1×10^6 K in all cases.

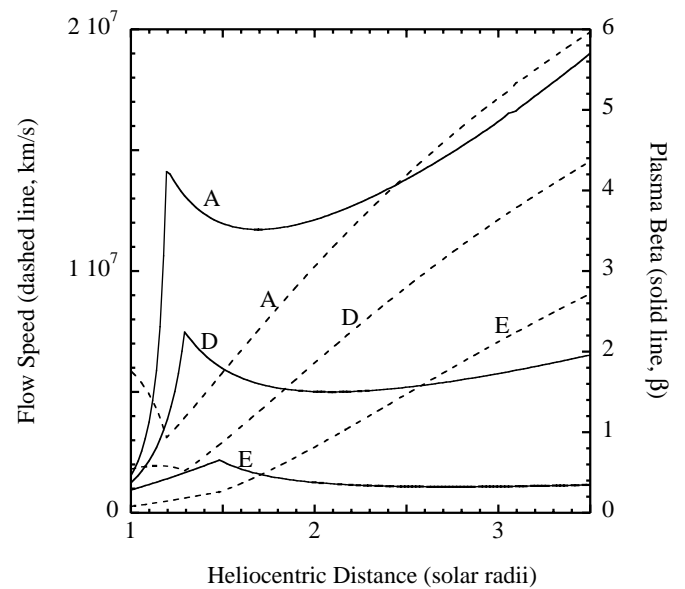


FIG. 12.—Plasma β (solid lines) in regions R2 and R3 for cases A, D, and E from Table 2, plotted along with the flow speeds for the same cases for comparison.

show here that it would not be appropriate to make such an assumption. Figure 12 shows β in R2 and R3 for the three examples A, D, and E, along with the associated flow speeds. The high-density, high- T_2 , high flow speed solution A leads to $\beta > 1$ everywhere in R2 and R3 except very near the base. Conversely, the low-density, low- T_2 , low flow speed solution E leads to $\beta < 1$ everywhere in R2 and R3.

The densities in E are still a little higher than the empirical densities shown in Table 1, so it might be concluded that $\beta_2 = O(1)$ in the boundary flow between the helmet and brightness boundaries of streamers. The solutions shown here, however, are for isothermal flow that does not couple density at the base to the flow speed. In addition, we have made no effort to display sets of solutions with constant mass flux, as might be preferred for comparison with solar wind data. Without putting more physics into the model and undertaking an extensive survey of solution space, it is difficult to make any specific conclusions about the order of magnitude of β in R2 based on the present model. It can only be said that plausible solutions can be found that have both $\beta_2(r) < 1$ and $\beta_2(r) > 1$.

Conversely, outside the brightness boundary, where there is typical low-density coronal hole flow, it is already well known that $\beta \ll 1$. Later we will invoke this result when discussing how to relax the restriction shown in Figure 2 to a radial brightness boundary.

4.4. Expansion Time and Gravitational Settling

It has been suggested (Raymond et al. 1998) that gravitational settling produces an overall depletion of heavy elements at large heights in the closed field regions of streamers or in the helmets. Raymond et al. also suggest that settling is less important or unimportant in streamer legs because of some form of mixing that refreshes the material in the legs on a timescale of 1 day or less. We can evaluate this suggestion by computing the time-to-height relation for the flow in R2 and R3.

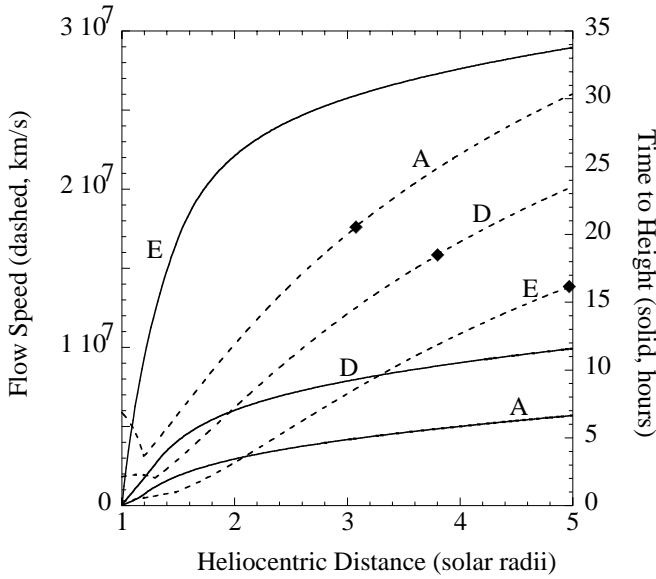


FIG. 13.—Time-to-height ratio (solid lines), as computed according to eq. (49), for cases A, D, and E from Table 2. Also plotted is the flow for the same cases for comparison. Critical points in the flow speed are indicated by filled diamonds.

The time for a parcel of plasma to reach a given height, τ , is given by

$$\tau(r_1) = \int_{r_0}^{r_1} [dr/V_2(r)] . \quad (49)$$

This time is plotted in Figure 13 for examples A, D, and E, along with the flow speed and the critical points, out to $5 R_\odot$. It is seen that A and D profiles lead to times of much less than 1 day to reach $5 R_\odot$, while E leads to times of more than 1 day. The choice of $5 R_\odot$ is not arbitrary; above this height the plasma is effectively collisionless even in the high-density plasma of streamers (Suess et al. 1999c). It was reported in Raymond et al. (1998) that the gravitational settling time in the helmet is a “few days.” Given that result, it appears that flow speeds like those in example E can lead to significant gravitational settling while the other two examples would not. The empirical flow speed inside streamers has been reported to be rather low, similar to that in E (e.g., Poletto et al. 2002), so it is possible that gravitational settling will have to be examined in more detail. This is beyond the scope of the present model and will entail a solution of the multifluid equations like that described, for example, by Hu, Esser, & Habbal (2000).

5. DISCUSSION OF SOLUTIONS

The first result we show is the evolutionary track of a streamer under increasing temperature inside the helmet, in Figure 8. There were several specific results associated with this. First, for a given width of the streamer as specified in terms of \mathcal{R} , there is a maximum temperature and an associated maximum helmet height above which there is no solution. P68 interpreted this as the point beyond which the magnetic field and plasma adjacent to the helmet could no longer contain the helmet. We note, however, that for temperatures above this point \mathcal{R} will begin increasing, corre-

sponding to a decreasing helmet height and width. As the temperature further increases, both the width and height now decrease until the helmet disappears. This final helmet disappearance is absolute and occurs at a temperature of $\sim 3.5 \times 10^6$ K in the $\tau = 1$ case. We find that although the result is parameter dependent, it is generally true that this model predicts no helmet heights above $3.0 R_\odot$ and an absolute maximum temperature for the existence of a helmet of $\sim 3.5 \times 10^6$ K. However, this is a specific result for an isothermal helmet. First, it is possible for much higher temperatures to exist in active regions within helmets. Second, it may be possible for a streamer to exist in the complete absence of a helmet.

The next result we show is the possible occurrence of stagnation flow in the vicinity of the helmet cusp, depending on the flow parameters. This is a result anticipated by Vásquez et al. (1999). Their solution was for solar wind flow in a predetermined magnetic field geometry that included both the closed field lines in the helmet and open field lines near and far from the helmet. They found fast-wind flow far from the helmet, but the possibility of two solutions near the helmet cusp where $f'(r)$ is large. One of these solutions was close to the fast-wind solution far from the helmet. The other solution exhibited the stagnation flow. They note that the stagnation flow can lead to locally significant gravitational settling and an influence on elemental abundances in the resulting solar wind. Here we have investigated the conditions under which stagnation flow exists, where we now interpret this term to mean cases in which there is a local maximum in $V_2(r)$ in R2. Stagnation flow is found here to occur only when the maximum value of $V_2(r) \gtrsim 30 \text{ km s}^{-1}$ and the helmet is domed rather than cusped. The absence of stagnation in Figure 9 is due to the generally small flow speeds. The strong stagnation in Figure 10 results from the flow speed at the base always being greater than 50 km s^{-1} and the domed helmet with its associated locally large $f'(r)$. We expect the stagnation in Figure 10 would have disappeared for slightly larger T_1 than in example C, but a standing shock appears in this case and we are unable to give a quantitative solution. The stagnation in Figure 11 disappears below flow speeds of $\sim 20 \text{ km s}^{-1}$. Returning to the model of Vásquez et al. (1999), we see they have flow speeds that reach more than 100 km s^{-1} adjacent to the helmet. Other multifluid slow solar wind models often have very low flow speeds at the base of the corona and empirical results suggest flow speeds less than 50 km s^{-1} inside the brightness boundary below $2 R_\odot$ (Poletto et al. 2002). Therefore, the importance of stagnation cannot be clearly decided at this time. It is possible, however, that stagnation is only important, if at all, for very short and broad helmet structures. A quantitative answer to this question awaits multifluid models with greatly improved treatments of the energetics of the flow.

Another issue we raise in § 4 is the possible existence of standing shock waves in R2. These occur in this model because the flow starts out supersonic at the base or becomes supersonic somewhere in R2 and then has to match with subsonic flow in R3. There are strong empirical results that the flow is subsonic in R3 (Poletto et al. 2002). Weaker empirical results have not given any suggestion of supersonic flow in R2. The possibility of supersonic flow in R2 exists, however, because of the large values of $f'(r)$ that must occur in compact streamers. If the shocks occur, the model described here implies a finite change in $A_1(r)$ and

$A_2(r)$ at the shock. This is a consequence of neglecting the magnetic field in R1 and computing only the average values of the variables for any given height. Nevertheless, it implies that the consequences of such a shock might be detectable, buried inside the brightness boundary.

Finally, we briefly considered whether stagnation might locally enhance gravitational settling and modify elemental abundances in the solar wind. It is impossible to give any detailed answer to this question without a multifluid model. However, we computed the time-to-height profiles for some of the solutions we found and showed them in Figure 13. These profiles show that when stagnation occurs, the large flow speeds around the $V_2(r)$ maximum in R2 reduce the advection times and imply that gravitational settling will be of little importance. The main cases in which gravitational settling looks to be important are when the flow speed is small throughout R2. To understand when $V_2(r)$ is small everywhere requires, again, a much more detailed analysis of the energetics than is possible here.

6. DISCUSSION OF THE MODEL

This model, although geometrically simple, is seen to retain the most important aspects of helmet containment and the dynamics of flow inside the brightness boundary. Its particular weaknesses are the simple treatment of energetics and the assumption of a radial-brightness boundary. We believe both of these weaknesses can be removed without eliminating the geometric and mathematical simplicity of the model.

The energetics is most simply addressed by expanding the one-dimensional equations of motion (eqs. [1]–[9]) to include thermal conduction, energy and momentum sources, and/or multiple fluids (electron-proton gas, ions). For example, a corresponding set of one-dimensional equations for a four-fluid turbulence-driven wind has been solved by Hu et al. (2000), where the geometry has been taken into consideration through a spreading function defined as in equation (47), but without the coupling to adjacent regions that we have described. Hu et al. solved the equations by introducing time dependence, starting with an arbitrary initial state, and allowing the flow to relax in time to the steady state solution. Solution methods to this type problem are described in detail by Hu et al. (2000) and Suess (1982). The difference in solving the equivalent problem to that described in equations (1)–(9) is small. The number of equations is increased only through the coupling with R1.

It is possible to relax the restriction to a radial brightness boundary because of the character of conditions in coronal holes. Consider the geometry illustrated in Figure 14, which is a generalization of that shown in Figure 3 to include a nonradial brightness boundary and a new region R4 of cross section $A_4(r)$. R1, R2, and R3 are defined in the same way as in Figure 3, while R4 is imagined to be low- β coronal hole flow. The outer boundary to R4 is imagined to be radial, a choice guided by the numerical results shown in Figure 2. In coronal hole flow, $\beta \ll 1$ and it is possible to completely neglect the flow to $O(1)$ when computing the

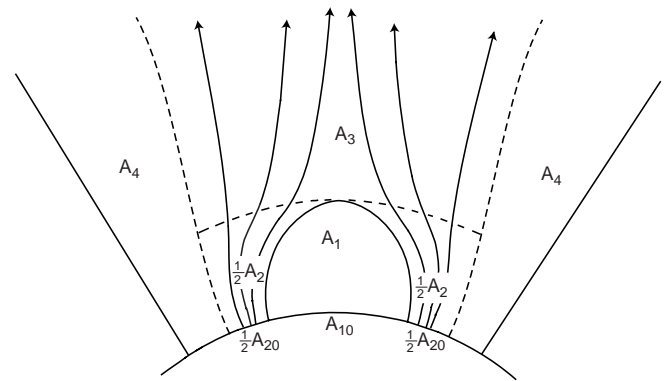


FIG. 14.—Geometry proposed for the streamer model to relieve the restriction of a radial-brightness boundary. A1, A2, and A3 are defined in Fig. 3, and A4 is introduced here, outside the brightness boundary (dashed lines).

transverse pressure balance. This means that the brightness boundary between R4 and R2 or R3 satisfies the pressure balance given by

$$\left. \frac{B_4(r)^2}{8\pi} \right|_{r \leq r_h} = \frac{B_2(r)^2}{8\pi} + 2N_2(r)kT_2(r), \quad (50a)$$

$$\left. \frac{B_4(r)^2}{8\pi} \right|_{r \geq r_h} = \frac{B_3(r)^2}{8\pi} + 2N_3(r)kT_3(r). \quad (50b)$$

Equation (50) gives $A_4(r)$ and the shape of the brightness boundary without resorting to a full multidimensional model. The solution to the expanded set of steady state equations would involve an additional iteration, since it would be impossible to write down the critical point conditions in R3 alone as was done here in § 3.1. Therefore, it probably would be easiest to solve these expanded equations in the same way as suggested above for incorporating a generalized energy equation.

7. SUMMARY AND CONCLUSIONS

We have described a simple one-dimensional analytic model of streamer helmets (the closed magnetic field region) and flow between the helmet and the streamer brightness boundary. This model is able to recover the shape of the helmet, show the evolution of the helmet under a slowly increasing temperature, and show the maximum heights and widths of the helmet. It is also able to recover the stagnation flow that can occur in the vicinity of the helmet cusp and show under what conditions stagnation flow exists. Finally, we describe how this model can be easily generalized to remove its most important restrictions.

We would like to thank Roger Kopp for suggesting this approach to the problem of streamer and helmet modeling. This work was supported by the NASA *Ulysses*/SWOOPS project and by a NASA Living With A Star data analysis, theory, and modeling grant.

REFERENCES

- Aellig, M. R., Lazarus, A. J., & Steinberg, J. T. 2001, *J. Geophys. Res.*, 28, 2767
 Gary, G. A. 2001, *Sol. Phys.*, 203, 71
 Hu, Y.-Q., Esser, R., & Habbal, S. R. 2000, *J. Geophys. Res.*, 105, 5093
 Kopp, R. A., & Holzer, T. E. 1976, *Sol. Phys.*, 49, 43
 Leer, E., & Holzer, T. E. 1990, *ApJ*, 358, 680
 Li, J., et al. 1998, *ApJ*, 506, 431
 Parker, E. N. 1963, *Interplanetary Dynamical Processes* (New York: Interscience)
 Pneuman, G. 1968, *Sol. Phys.*, 3, 578
 Poletto, G., Suess, S. T., Biesecker, D. A., Esser, R., G. Gloeckler, K., Y.-K., & Zurbuchen, T. H. 2002, *J. Geophys. Res.*, in press

- Raymond, J., Sulieman, R., van Ballegooijen, A., & Kohl, J. 1998, in Proc. 31st ESLAB Symp., Correlated Phenomena at the Sun, in the Heliosphere, and in Geospace (ESA SP-415; Noordwijk: ESA), 383
- Steinolfson, R. S., Suess, S. T., & Wu, S. T. 1982, *ApJ*, 255, 730
- Suess, S. T. 1982, *ApJ*, 259, 880
- Suess, S. T., Gary, G. A., & Nerney, S. F. 1999a, in AIP Conf. Proc. 471, Solar Wind Nine, ed. S. R. Habbal, R. Esser, J. V. Hollweg, & P. A. Isenberg (New York: AIP), 247
- Suess, S. T., & Nerney, S. F. 1999, in Proc. 9th European Meeting on Solar Physics: Magnetic Fields and Solar Processes (ESA SP-448; Noordwijk: ESA), 1101
- Suess, S. T., & Smith, E. J. 1996, *Geophys. Res. Lett.*, 23, 3267
- Suess, S. T., Wang, A.-H., Wu, S. T., & Nerney, S. F. 1999b, *Space Sci. Rev.*, 87, 323
- Suess, S. T., Wang, A.-H., Wu, S. T., Poletto, G., & McComas, D. J. 1999c, *J. Geophys. Res.*, 104, 4697
- Vásquez, A. M., van Ballegooijen, A. A., & Raymond, J. C. 1999, in AIP Conf. Proc. 471, Solar Wind Nine, ed. S. R. Habbal, R. Esser, J. V. Hollweg, & P. A. Isenberg (New York: AIP), 243
- Wang, A.-H., Wu, S. T., Suess, S. T., & Poletto, G. 1998, *J. Geophys. Res.*, 103, 1913